

WILDLAND FIRE DYNAMICS

Wildland fires are among the most complicated environmental phenomena to model. Fire behavior models are commonly used to predict the direction and rate of spread of wildland fires based on fire history, fuel, and environmental conditions; however, more sophisticated computational fluid dynamic models are now being developed. The quantitative analysis of fire as a fluid dynamic phenomenon embedded in a highly turbulent flow is beginning to reveal the combined interactions of the vegetative structure, combustion-driven convective effects, and atmospheric boundary layer processes. This book provides an overview of the developments in modeling wildland fire dynamics and the key dynamical processes involved. Mathematical and dynamical principles are presented, and the complex phenomena that arise in wildland fire are discussed. Providing a state-of-the-art survey, it is a useful reference for scientists, researchers, and graduate students interested in wildland fire behavior from a broad range of fields.

KEVIN SPEER is a professor and Director of the Geophysical Fluid Dynamics Institute at Florida State University, with experience in field and laboratory measurements of turbulent geophysical flows. He recently developed a new program in Fire Dynamics at Florida State University that combines the fields and faculty of numerous departments, including Earth, Ocean, and Atmospheric Sciences; Mathematics; Scientific Computing; Statistics; Physics; and Engineering.

SCOTT GOODRICK is a research meteorologist with the US Forest Service Southern Research Station and serves as Director of the Station's Center for Forest Health and Disturbance in Athens, GA. He has been working as a research scientist with the Forest Service, specializing in fire-atmosphere interactions and smoke management for 18 years. Prior to joining the US Forest Service, he spent four years as the fire weather meteorologist for the state of Florida, helping to develop their Fire Management Information System.

WILDLAND FIRE DYNAMICS

Fire Effects and Behavior from a Fluid Dynamics Perspective

Edited by

KEVIN SPEER

Florida State University

SCOTT GOODRICK

US Forest Service



CAMBRIDGE
UNIVERSITY PRESS

CAMBRIDGE
UNIVERSITY PRESS

University Printing House, Cambridge CB2 8BS, United Kingdom

One Liberty Plaza, 20th Floor, New York, NY 10006, USA

477 Williamstown Road, Port Melbourne, VIC 3207, Australia

314–321, 3rd Floor, Plot 3, Splendor Forum, Jasola District Centre, New Delhi – 110025, India

103 Penang Road, #05–06/07, Visioncrest Commercial, Singapore 238467

Cambridge University Press is part of the University of Cambridge.

It furthers the University's mission by disseminating knowledge in the pursuit of education, learning, and research at the highest international levels of excellence.

www.cambridge.org

Information on this title: www.cambridge.org/9781108498555

DOI: [10.1017/9781108683241](https://doi.org/10.1017/9781108683241)

© Kevin Speer and Scott Goodrick 2022

This publication is in copyright. Subject to statutory exception and to the provisions of relevant collective licensing agreements, no reproduction of any part may take place without the written permission of Cambridge University Press.

First published 2022

A catalogue record for this publication is available from the British Library.

ISBN 978-1-108-49855-5 Hardback

Additional resources for this publication at www.cambridge.org/9781108498555

Cambridge University Press has no responsibility for the persistence or accuracy of URLs for external or third-party internet websites referred to in this publication and does not guarantee that any content on such websites is, or will remain, accurate or appropriate.

2

The Structure of Line Fires at Flame Scale

SALMAN VERMA, MOHAMED AHMED, AND ARNAUD TROUVÉ

2.1 Introduction

The dynamics of wildland fires involve multi-physics phenomena occurring at multiple scales. Different length scales are believed to play a role in fire behavior: the vegetation scales, denoted $L_{vegetation}$, that characterize the biomass fuel; the flame scales represented by a characteristic flame height and width, L_{flame} and W_{flame} , as well as the length of the fire line, $L_{fireline}$, that characterize the combustion and heat transfer processes; the geographical scales, $L_{topography}$ and L_{land_cover} , that characterize the terrain topography ($L_{topography}$ is the characteristic scale for change in elevation of the terrain) and land cover (L_{land_cover} is the characteristic scale for change in vegetation type and/or surface fuel load); and the meteorological scales represented by the depth of the atmospheric boundary layer, L_{ABL} , that characterize atmospheric conditions. In addition, the fire plume has scales that can be represented by a characteristic height and width, L_{plume} and W_{plume} ; the plume scales take a large range of values as they grow from flame scales to geographical scales and then to meteorological scales. In wildland fire problems, $L_{vegetation}$ is on the order of a few millimeters or centimeters; L_{flame} and W_{flame} are on the order of a few meters; $L_{fireline}$, $L_{topography}$, and L_{land_cover} are typically on the order of a few tens or hundreds of meters; and L_{ABL} is on the order of kilometers.

Computational Fluid Dynamics (CFD) models have the potential to provide detailed information on the interactions between physical phenomena occurring at all these different scales. However, because of computational cost, the domain of application of CFD models is typically limited to a particular range of scales. Thus, current CFD-based wildland fire models are scale-specific and belong to one of the following three classes (see Figure 2.1): combustion solvers aimed at describing

Results presented in this chapter were produced in the past few years through projects financially supported by the U.S. Forest Service, Rocky Mountain Research Station, and by FM Global. These projects were also supported by supercomputing resources made available by the University of Maryland (<http://hpcc.umd.edu>) and by the National Science Foundation (XSEDE Program, Grant #TG-CTS140046).

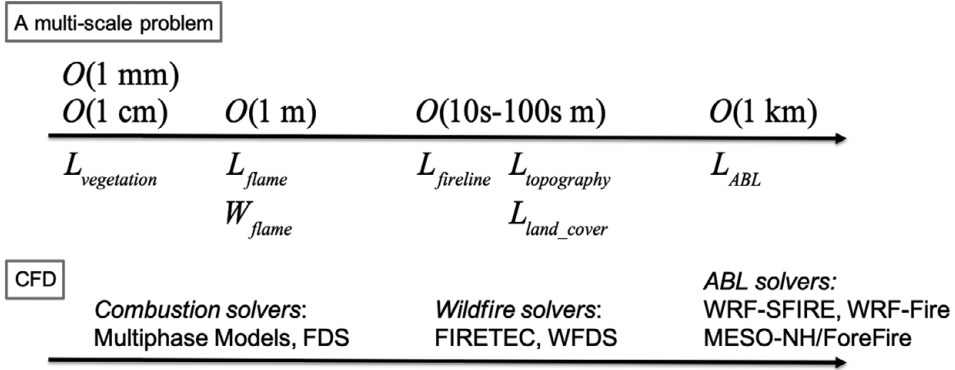


Figure 2.1 The different classes of CFD models used for wildland fire spread simulations: combustion solvers resolve dynamics at the vegetation and flame scales; wildfire solvers resolve dynamics at the fireline and geographical scales; atmospheric boundary layers (ABL) solvers resolve dynamics at the meteorological scales.

the coupling between pyrolysis, combustion, radiation, and flow occurring at the vegetation and flame scales; wildfire solvers aimed at describing the coupling between combustion and flow occurring at fire line scales and/or geographical scales; and atmospheric boundary layer solvers aimed at describing the coupling between combustion and flow occurring at meteorological scales.

Examples of combustion solvers that have been developed for wildland fire dynamics applications include a group of models known as multiphase models (Porterie et al. 2000; Morvan and Dupuy 2001, 2004). These solvers use a computational grid resolution of order 1–10 cm and provide a fine-grained treatment of the pyrolysis, combustion, and heat transfer processes that are responsible for flame spread through a first principles-based model. Simulations with these solvers are typically performed in small domains (a few tens of meters in two-dimensional simulations or a few meters in three-dimensional simulations). Other examples of combustion solvers include FDS¹ and FireFOAM²; these solvers are well-established fire models that are primarily used for building fire applications; they have also been adapted for wildland fire applications.

Examples of wildfire solvers include FIRETEC (Linn and Cunningham 2005; Canfield et al. 2014) and WFDS (Mell et al. 2007) (WFDS is based on FDS). These solvers use a computational grid resolution of order 1 m and provide a coarse-grained treatment of unresolved vegetation-scale and flame-scale processes through a simplified (but physics-based) combustion model. Simulations with

¹ Fire Dynamics Simulator (FDS), developed by the National Institute of Standards and Technology, n.d. <https://pages.nist.gov/fds-smv/> (last accessed September 29, 2019).

² FireFOAM, developed by FM Global, n.d. <https://github.com/fireFoam-dev> (last accessed September 29, 2019).

these solvers are typically performed in intermediate-size field-scale domains (e.g. 1 km in size).

Examples of atmospheric boundary layer (ABL) solvers that have been developed for wildland fire dynamics applications include WRF-SFIRE and WRF-Fire (Clark et al. 2004; Mandel et al. 2011; Coen et al. 2013; Kochanski et al. 2013), as well as MESO-NH/ForeFire (Filippi et al. 2009, 2013). These solvers use a computational grid resolution of order 10–100 m and provide a macroscopic-level treatment of unresolved vegetation-scale, flame-scale, fireline-scale, and small-geographical-scale processes through a parametrized semi-empirical rate-of-spread fire model. Simulations with ABL solvers are typically performed in arbitrary-size field-scale domains (from a few kilometers to several tens of kilometers and beyond). A strength of ABL solvers is that they are integrated with research-level or operational-level numerical weather prediction capabilities (i.e. WRF and MESO-NH) and therefore incorporate detailed descriptions of the fuel maps, topographic maps, and weather conditions.

In the present chapter, we focus on the viewpoint adopted in combustion solvers and use high-resolution computational modeling to bring basic information on the coupling between combustion, radiation, and turbulent flow processes occurring at flame scale. This viewpoint is typically adopted in standalone theoretical studies or in joint computational–experimental studies of controlled laboratory-scale flames. In addition, we limit the scope of the discussion to a simplified configuration in which the flame is fueled by methane gas supplied at a prescribed flow rate. In this configuration, the heat release rate of the flame is controlled and the flame is stationary (i.e. non-spreading). It is worth emphasizing that a number of important features of wildland fires are left out of the present gas-fueled configuration; for instance: the presence of a complex and discontinuous system of vegetation fuel in the wildland in the form of discrete and disconnected particles of different shapes and sizes; the uncontrolled production of flammable vapors (i.e. the fuel) due to pyrolysis reactions occurring inside the vegetation fuel and driven by the gas-to-solid (convective and radiative) heat transfer; the typical cycle of ignition, pyrolysis and end-of-pyrolysis (due to a reduction in the gas-to-solid heat transfer) or burn-out (due to fuel depletion); and the displacement (i.e. the spreading) of the flame region. The study of gas-fueled configurations may be viewed as an intermediate step on the road to provide a basic understanding of the dynamics of wildland fires.

Furthermore, we focus in the present chapter on the line fire configuration. Line fires have a simplified structure (they are statistically two-dimensional) and are representative of the flame geometry found in wildland fire applications in which the fire may be viewed as a thin front that separates unburned and burned vegetation: the flame height and flame width, L_{flame} and W_{flame} , are on the order of a few meters, while the length of the fireline, $L_{fireline}$, is on the order of a few

tens or hundreds of meters (or more); we therefore have: $L_{fireline} \gg L_{flame}$ and $L_{fireline} \gg W_{flame}$. Thus, the line fire configuration may be viewed as a canonical configuration in wildland fire research (note that this is perhaps the only canonical configuration currently accepted in wildland fire research). In the following, we consider two variations of the line fire configuration: a first configuration in which the gas-fueled flame develops along a horizontal flat surface under controlled cross-flow conditions that represent wind; and a second configuration in which the gas-fueled flame develops along an inclined flat surface that represents sloped terrain. In the configuration with wind, the direction of the wind is taken as perpendicular to the line flame; in the configuration with slope, the direction of the slope is taken as perpendicular to the line flame.

2.2 The Dynamics of Line Fires

One of the most striking features of flames propagating over a vegetation bed in the presence of a cross-flow or along sloped terrain is the existence of two limiting flame regimes (Pagni and Peterson 1973; Morvan et al. 1998; Morvan and Dupuy 2004; Morvan 2011): the plume-dominated regime in which the flame is mostly detached from the bed, has a vertically tilted geometry and air entrainment is two-sided; and the wind-driven or slope-driven regime in which the flame is attached to the bed, has a boundary layer geometry and air entrainment is one-sided (see Figure 2.2). These two regimes correspond to different flame spread mechanisms

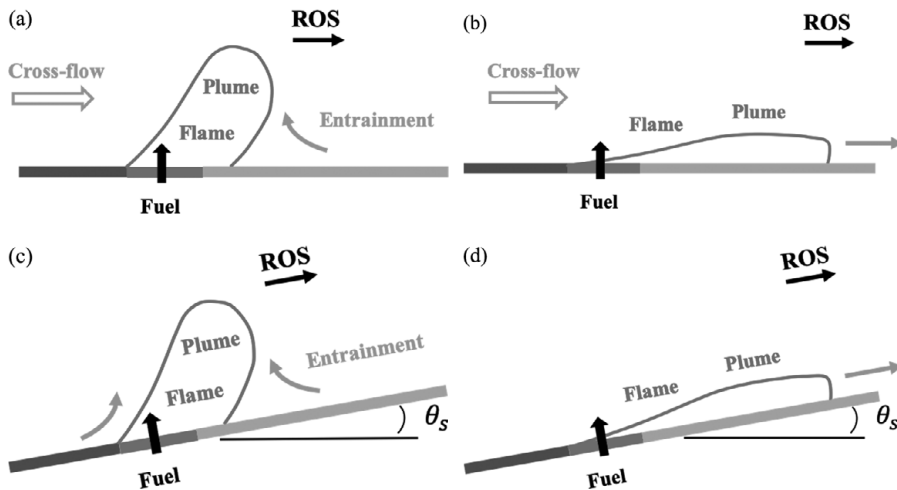


Figure 2.2 The different flame regimes found in wildland fire spread: (a) and (c) the detached flame regime; and (b) and (d) the attached flame regime. Cases (a) and (b) correspond to a configuration with wind; cases (c) and (d) correspond to a configuration with sloped terrain.

(and in particular different relative weights for radiative and convective heat transfer) and to different values of the rate of spread (ROS): in the plume-dominated regime, the surfaces that are downwind/upslope of the flame are exposed to an inflow of ambient air, that is, to convective cooling, and flames spreading in the downwind/upslope direction will therefore feature low-to-moderate values of ROS; in contrast, in the wind-driven or slope-driven regime, the surfaces that are downwind/upslope of the flame are exposed to an outflow of combustion gases, that is, to convective heating, and flames spreading in the downwind/upslope direction will therefore feature moderate-to-high values of ROS. Recent work has shed some new light on the importance of convective heating in controlling fire spread under conditions aided by wind or slope (Finney et al. 2013, 2015). Note also that the possible transition to the limiting wind-driven or slope-driven regime is believed to be a key factor, and possibly the main factor, in a special category of fire behavior known as “eruptive fires” (Viegas 2005; Dold and Zinoviev 2009): eruptive fires are characterized by large values of flame acceleration, high (and time-dependent) values of ROS, and flow and flame attachment to the ground surface (Dold and Zinoviev 2009). On a separate but related subject, variations in the flame structure and in downwind surface conditions similar to those observed in the case of vegetation fires (albeit without spread) have also been observed in the case of liquid pool fires (Lam and Weckman 2015a, 2015b; Hu 2017) and low-momentum gaseous flames (Tang et al. 2017) exposed to a cross-flow.

In the first configuration with wind (and without slope), the literature suggests that the flame structure is controlled by a non-dimensional number known as Byram’s convection number and noted N_C (Albini 1981; Raupach 1990; Nelson 1993; Morvan and Frangieh 2008; Nelson et al. 2012):

$$N_C = 2 \frac{(1 - \chi_{rad}) \dot{Q}' g}{(\rho_a c_{p,a} T_a) u_w^3} \quad (2.1)$$

where \dot{Q}' is the fire intensity (i.e. the rate of heat release due to combustion per unit length of the fireline), χ_{rad} the radiant fraction of the flame (i.e. the fraction of the energy released by combustion that is lost to the surroundings due to thermal radiation transport), g the magnitude of the gravity acceleration, ρ_a , $c_{p,a}$, and T_a the mass density, heat capacity (at constant pressure), and temperature of ambient air, respectively, and u_w the magnitude of the cross-wind velocity. The importance of N_C can be readily understood if one considers that the characteristic buoyant velocity of a line fire without wind is $w_B \sim (\dot{Q}' g / (\rho_a c_{p,a} T_a))^{(1/3)}$ (Yuan and Cox 1996); thus N_C gives an estimate of the relative strength of buoyant forces that drive the fire in the vertical direction, as measured by

w_B , and inertial forces that drive the fire in the direction tangent to the (horizontal) ground surface, as measured by u_w , $N_C \sim (w_B/u_w)^3$. High values of N_C correspond to a plume-dominated fire; low values of N_C correspond to a wind-driven fire. The literature suggests that the transition between the two flame regimes occurs for values of N_C between 2 and 10 (Morvan and Frangieh 2008; Nelson et al. 2012).

Note that the literature does not always recognize N_C as the main parameter to characterize the structure of line fires with wind and that alternative parameters, usually cast in the form of a Froude or a Richardson number, have also been proposed. For instance, the studies in Putnam (1965), Morvan and Dupuy (2004), and Nmira et al. (2010) use a Froude number as their main scaling parameter, $Fr = u_w^2 / (gL_{f,0})$, where $L_{f,0}$ is the vertical flame height of the line fire without wind. In many cases, these alternative scaling parameters are directly related to Byram's convection number: for instance, if one considers that the flame height of a line fire without wind (or slope) scales like $L_{f,0} \sim (\dot{Q}' / (\rho_a c_{p,a} T_a \sqrt{g}))^{(2/3)}$ (Yuan and Cox 1996), one finds that $Fr \sim N_C^{(-2/3)}$.

Furthermore, it is worth noting that a few recent studies have questioned the value of Byram's convection number as a controlling factor of wind-aided fire spread (Sullivan 2007; Morandini and Silvani 2010). The study in Sullivan (2007) considers a series of prescribed grassland fires conducted on flat terrain and finds no correlation between the measured rate of spread of the fire and N_C (note that under propagating fire conditions, the velocity u_w in Eq. (2.1) is replaced by the relative velocity ($u_w - ROS$)). Similarly, the study in Morandini and Silvani (2010) considers a series of prescribed vegetation fires conducted on sloped terrain, identifies two different flame spread regimes, but finds no correlation between observed fire behavior and N_C . These results are difficult to interpret: data presented in Sullivan (2007) and Morandini and Silvani (2010) correspond to field-scale studies that feature propagating fires under variable wind conditions and over vegetation beds with finite thickness, and, in such complex systems, the effects of N_C could be masked by the effects of other parameters or by experimental uncertainties. In addition, the data analysis presented in Morandini and Silvani (2010) may be questionable because, as pointed out in Nelson, (2015), under sloped terrain conditions, the expression of N_C should be modified to include a correction for the slope angle.

Our own results, presented in Sections 2.3 and 2.4, confirm the importance of Byram's convection number for gas-fueled line flames exposed to wind. These results come from an integral model based on the classical theory of buoyant plumes in the presence of wind; the integral analysis suggests that the plume tilt angle is uniquely determined by N_C . The results also come from fine-grained Large Eddy Simulation (LES) performed for different values of the cross-wind velocity,

u_w , and different values of the fire intensity, \dot{Q}' ; the LES results suggest that the transition between the detached and attached flame regimes occurs for values of N_C close to 1.

In the second configuration with slope (and without wind), the literature suggests that the flame structure is controlled by the slope angle, noted θ_s (θ_s is defined as the angle between the sloped surface and the horizontal plane, see Figure 2.2(c) and (d)). Low values of θ_s correspond to a plume-dominated fire; high values of θ_s correspond to a slope-driven fire. The literature suggests that the transition between the two flame regimes occurs for critical values of θ_s , noted $\theta_{s,critical}$, between 10 and 27 degrees (i.e. for values of the slope between 18 and 51%) (Drysdale and Macmillan 1992; Smith 1992; Woodburn and Drysdale 1998; Wu et al. 2000; Sharples et al. 2010). Similar to wind-driven fires, slope-driven fires are associated with an attached flame and plume geometry, and with large values of the rate of spread (values of ROS that are at least an order of magnitude larger than those observed in the plume-dominated regime). Slope-driven fires also feature strong unsteady effects and sustained flame acceleration, which suggests that, in the attached flame regime, ROS should be viewed as a time-dependent dynamical quantity (Viegas 2004).

The large variations in the observed values of the critical angle for transition between the detached and attached flame regimes are explained by the sensitivity of the line fire configuration to three-dimensional effects, in particular the presence or absence of lateral entrainment of air into the flame and plume regions. It is found that the transition to the attached flame regime is promoted by the presence of sidewalls that prevent lateral air entrainment, inhibit three-dimensional effects, and make the flame-flow configuration statistically two-dimensional: configurations with side walls correspond to lower values of $\theta_{s,critical}$ (Woodburn and Drysdale 1998; Sharples et al. 2010). These configurations are often referred to as “trenches” or “canyons” in the literature. In contrast, configurations without side walls feature strong edge effects, three-dimensional effects, and correspond to larger values of $\theta_{s,critical}$ (Dupuy et al. 2011; Huang and Gollner 2014).

The transition between the plume-dominated and slope-driven fire regimes is also associated with a change in the dominant mode of heat transfer that controls flame spread. It is found that, while radiation heat transfer tends to dominate under detached flame conditions, that is, at low values of θ_s , convection heat transfer tends to dominate under attached flame conditions, that is, at high values of θ_s (Dupuy and Maréchal 2011; Morandini et al. 2018). The dominant role of radiation and convection, at small and large values of the slope angle, respectively, can be explained in part by considering the flow direction in the vicinity of the flame: in the plume-dominated regime, the surface located upslope

of the flame is exposed to downslope flow of ambient air, that is, to a “reverse” flow and convective cooling; in contrast, in the slope-driven regime, the upslope surface is exposed to upslope flow of combustion gases, that is, to convective heating. Note that one of the important features of line fires in the presence of wind or slope is the asymmetry of the air entrainment process into the flame and plume regions: the air entrainment capacity is higher on the upwind/downslope side of the fire and lower on the downwind/upslope side; this imbalance in the air entrainment capacity acts to accentuate the deflection of the flame and plume.

In summary, in configurations with wind, the structure of line fires is characterized in terms of Byram’s convection number, N_C , while, in configurations with slope, the same structure is characterized in terms of the slope angle, θ_s . The question of how these two viewpoints can be reconciled is not addressed in the literature and remains an open question. A possible approach to reconcile the viewpoints based on N_C and θ_s can, however, be derived from the work presented in Nelson (2002): in Nelson (2002), the effects of slope are first represented through the introduction of an effective wind velocity, noted $u_{w, Eff}$; the velocity $u_{w, Eff}$ is then treated as the projection on the sloped surface of the characteristic velocity of the line fire in the vertical direction; and finally this characteristic velocity is taken as the reference buoyant velocity w_B , obtained in the absence of wind and slope. In the absence of wind, one writes (Nelson 2002):

$$u_{w, Eff} = w_B \times \sin(\theta_s) = \left[C_b \times \left(\frac{(1 - \chi_{rad}) \dot{Q}' g}{(\rho_a c_{p, a} T_a)} \right)^{(1/3)} \right] \times \sin(\theta_s), \quad (2.2)$$

where C_b is a model coefficient. This expression can now be substituted into Eq. (2.1) and thereby produce an estimate of Byram’s convection number in the case of sloped terrain (and without wind):

$$N_C = \frac{2}{(C_b \times \sin(\theta_s))^3}. \quad (2.3)$$

This argument suggests that the transition between the detached and attached flame regimes is uniquely controlled by the slope angle θ_s and is thereby consistent with reported observations and implicit assumptions made in the literature. Our own results, presented in Sections 2.3 and 2.4, confirm the importance of the slope angle for gas-fueled line flames evolving along an inclined surface (and without lateral air entrainment). These results come from fine-grained LES performed for different values of the slope angle, θ_s ; the LES results suggest that the transition between the detached and attached flame regimes occurs for values of θ_s close to 24 degrees.

2.3 Integral Model

We now turn to a brief description of the integral model used to develop a simple scaling analysis of the structure of line fires in wind-aided configurations (without slope). This model is based on the classical theory of weak buoyant plumes in the presence of wind and includes modifications introduced to describe strong plume effects (i.e. effects of large variations in mass density) as well as combustion effects in the near-field flame region. The model combines ideas developed in the atmospheric dispersion research community (Hoult et al. 1969; Krishnamurthy and Hall 1987), the wildland fire research community (Albini 1981; Mercer and Weber 1994; Nelson et al. 2012), and the combustion research community (Escudier 1972, 1975).

The model solves for the mean flame and plume structure through integral equations that express conservation of mass, vertical and horizontal momentum, heat, and fuel and oxygen mass. The model assumes steady state and top-hat profiles inside the flame and plume (all quantities are implicitly averaged in time and in space across the thickness of the flame/plume). The unit vector \vec{s} of coordinates $(\cos(\theta), \sin(\theta))$ marks the orientation of the centerline of the flame and plume (see Figure 2.3). We write:

$$\frac{d}{ds} (\dot{m}'_p) = 2\rho_a v_e \tag{2.4}$$

$$\frac{d}{ds} (\dot{m}'_p u_p \sin(\theta)) = (\rho_a - \rho_p) 2bg \tag{2.5}$$

$$\frac{d}{ds} (\dot{m}'_p u_p \cos(\theta)) = \frac{d}{ds} (\dot{m}'_p) u_w \tag{2.6}$$

$$\frac{d}{ds} (\dot{m}'_p c_p T_p) = \frac{d}{ds} (\dot{m}'_p) c_p T_a + (1 - \chi_{rad}) \dot{\Omega}''_F \Delta H_F \tag{2.7}$$

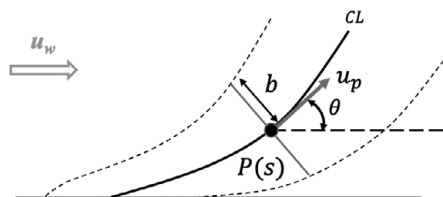


Figure 2.3 Integral model used to describe the mean flame/plume geometry in wind-aided configurations. The model calculates the variations of the half-thickness, b , inclination angle, θ , and relevant properties (e.g. the velocity u_p) as a function of the arc length, s , measured along the centerline of the flame and plume.

$$\frac{d}{ds} \left(\dot{m}'_p Y_{F,p} \right) = -\dot{\Omega}''_F \quad (2.8)$$

$$\frac{d}{ds} \left(\dot{m}'_p Y_{O_2,p} \right) = \frac{d}{ds} \left(\dot{m}'_p \right) Y_{O_2,a} - r_s \dot{\Omega}''_F, \quad (2.9)$$

where \dot{m}'_p is the mass flow rate (per unit length of the fireline) in the direction \vec{s} , v_e is a characteristic velocity used to quantify air entrainment into the flame/plume, u_p the flow velocity in the direction \vec{s} , ρ_p the mass density, c_p the heat capacity at constant pressure (assumed constant), T_p the temperature, $\dot{\Omega}''_F$ the fuel mass reaction rate (defined as the volumetric fuel mass reaction rate averaged across the thickness of the flame/plume), ΔH_F the heat of combustion (per unit mass of fuel), $Y_{F,p}$ the fuel mass fraction, $Y_{O_2,p}$ the oxygen mass fraction, $Y_{O_2,a}$ the oxygen mass fraction in ambient air, and r_s the stoichiometric oxygen-to-fuel mass ratio in the assumed global combustion equation, $F + r_s O_2 \rightarrow (1 + r_s)P$ (1 kg of fuel F reacts with r_s kg of oxygen O_2 to yield $(1 + r_s)$ kg of products P). By definition, we have $\dot{m}'_p = \rho_p (2b)u_p$, with ρ_p related to T_p through the ideal gas law, $\rho_p \approx \rho_a (T_a/T_p)$.

The corresponding kinematic equations that give the spatial coordinates (x_c , z_c) of the point $P(s)$ along the centerline of the flame and plume are:

$$\frac{d}{ds} (x_c) = \cos (\theta), \quad (2.10)$$

$$\frac{d}{ds} (z_c) = \sin (\theta). \quad (2.11)$$

Equations (2.5) and (2.6) assume that the entrainment of ambient air into the flame and plume regions has no net effect on vertical momentum and has a net effect on horizontal momentum that is proportional to the wind velocity. Note that these assumptions are not consistent with the asymmetry of the air entrainment process noted in Section 2.2; this asymmetry is expected to result in a net negative force in the vertical direction as well as a net positive force in the downwind direction. These effects are simply neglected in the present formulation.

An alternative formulation for Eqs. (2.5) and (2.6) is often adopted in the literature:

$$\frac{d}{ds} \left(\dot{m}'_p u_p \right) = \frac{d}{ds} \left(\dot{m}'_p \right) (u_w \cos (\theta)) + (\rho_a - \rho_p) 2bg \sin (\theta), \quad (2.12)$$

$$\left(\dot{m}'_p u_p \right) \frac{d\theta}{ds} = -\frac{d}{ds} \left(\dot{m}'_p \right) (u_w \sin (\theta)) + (\rho_a - \rho_p) 2bg \cos (\theta). \quad (2.13)$$

Equations (2.4)–(2.9) or Eqs. (2.4), (2.7)–(2.9), (2.12), and (2.13) require a submodel for air entrainment and a submodel for combustion. The submodel for the turbulent air entrainment velocity is taken from Hoult et al. (1969):

$$v_e = (\alpha|u_p - u_w \cos(\theta)| + \beta|u_w \sin(\theta)|) \times \left(\frac{\rho_p}{\rho_a}\right)^{(1/2)}, \quad (2.14)$$

where α and β are model coefficients taken from Mercer and Weber (1994): $\alpha = 0.16$ and $\beta = 0.5$. The expression in Eq. (2.14) assumes two mechanisms for air entrainment: a first mechanism due to the differential velocity between the plume and the ambient wind in the direction \vec{s} , $(u_p - u_w \cos(\theta))$; and a second mechanism due to the differential velocity between the plume and the ambient wind in the direction perpendicular to \vec{s} , $(u_w \sin(\theta))$. The last term in the expression for v_e , $(\rho_p/\rho_a)^{(1/2)}$ is a modification proposed in Escudier (1972) in order to account for strong density variations.

The submodel for combustion is similar to the formulation proposed in Escudier (1972, 1975):

$$\dot{\Omega}_F'' = GER \times \left(\frac{2\rho_a v_e \times Y_{O_2,a}}{r_s}\right), \quad (2.15)$$

where GER is a model coefficient that represents a global equivalence ratio. The submodel assumes that the rate of combustion is mixing-limited and controlled by air entrainment: in Eq. (2.15), the product $(2\rho_a v_e \times Y_{O_2,a})$ is the local flux of oxygen mass entrained into the flame region; if all of this oxygen mass is consumed by combustion, we then have $\dot{\Omega}_F'' = (2\rho_a v_e \times Y_{O_2,a})/r_s$; and we thus see that in Eq. (2.15), GER simply measures the fraction of the entrained oxygen mass that is participating in the combustion process. The literature suggests that, under many conditions, the global equivalence ratio inside the flame region remains close to 0.1 and we therefore assume in the model that GER can be treated as a constant, $GER = 0.1$. Finally, it is worth noting that the combustion model in Eq. (2.15) is only applied in the flame region, identified by the condition $Y_F > 0$; when Y_F becomes negative, the model switches to the inert plume equations and uses $\dot{\Omega}_F'' = 0$.

Figure 2.4 presents representative results obtained with the integral model. The model is applied to a laboratory-scale configuration corresponding to a methane line burner characterized by a low value of the fire intensity, $\dot{Q}' = 100 \text{ kW m}^{-1}$, and a small burner width, $w_{burner} = 5 \text{ cm}$. The center of the burner is located at $(x, z) = (0, 0)$; the ground surface is horizontal, $\theta_s = 0$. Figure 2.4(a–c) presents results obtained with different values of the horizontal wind velocity, $u_w = 0.75, 1.5, \text{ and } 3 \text{ m s}^{-1}$, corresponding to different values of Byram's convection number, $N_C = 10.2, 1.3, \text{ and } 0.16$, respectively. In the plots, the thick black solid line

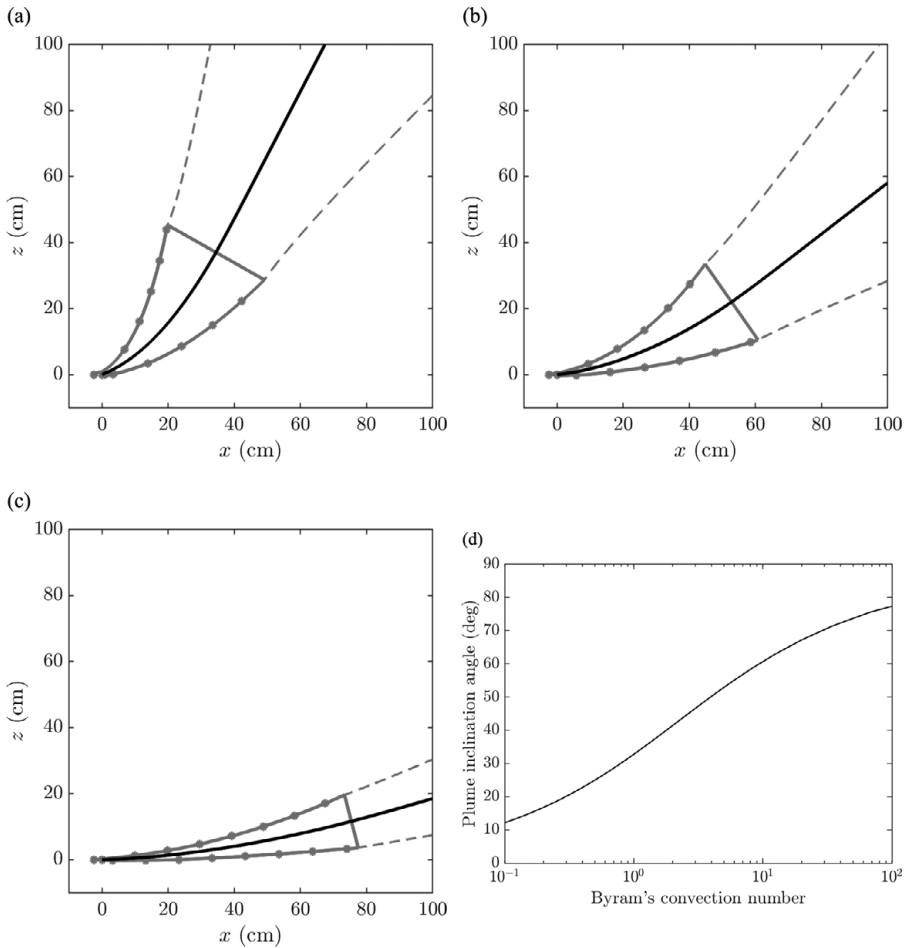


Figure 2.4 Simulations of the change in flame/plume structure with wind velocity, as predicted by the integral model. Flame/plume orientation and thickness simulated for different values of the crosswind velocity: (a) $u_w = 0.75 \text{ m s}^{-1}$; (b) $u_w = 1.5 \text{ m s}^{-1}$; (c) $u_w = 3 \text{ m s}^{-1}$. (d): variations of the asymptotic value of the plume inclination angle, θ_∞ , with Byram's convection number, N_C .

represents the location of the flame/plume centerline, that is, the location of the points P of coordinates (x_c, z_c) ; the red solid line represents the location of the edges of the flame region, defined as the region where $Y_F > 0$; the red dashed line represents the location of the edges of the plume region, defined as the region where $(T_p - T_a) > 50 \text{ K}$. As expected, the model shows that at low velocities (i.e. at large values of N_C), the line fire features a vertically tilted geometry, while at high velocities (i.e. at low values of N_C), the fire features a horizontal geometry. Note that the integral model does not include ground surface effects and implicitly assumes that the flame and plume are evolving far from solid boundaries; this is

clearly a serious limitation (and one that cannot be easily overcome) and, in its present form, the model is limited to qualitative use for physical insight and for the identification of controlling parameters.

One interesting result in Figure 2.4(a–c) is that, while the inclination angle θ varies significantly in the flame region, it is seen to achieve a constant asymptotic value in the plume region. We call θ_∞ this value and find that: for $u_w = 0.75 \text{ m s}^{-1}$, $\theta_\infty \approx 61^\circ$; for $u_w = 1.5 \text{ m s}^{-1}$, $\theta_\infty \approx 36^\circ$; and for $u_w = 1.5 \text{ m s}^{-1}$, $\theta_\infty \approx 15^\circ$. Based on this observation, one can develop a simplified analysis of the governing equations in Eqs. (2.4)–(2.9) valid in the far field region of the plume, where $\rho_p \approx \rho_a$, and derive the following solution:

$$b = \sin(\theta_\infty)(\alpha \sin(\theta_\infty) + \beta \cos(\theta_\infty)) \times s \tag{2.16}$$

$$u_p = \frac{u_w}{\cos(\theta_\infty)} \tag{2.17}$$

$$(T_p - T_a) = \left(\frac{T_a u_w^2}{g}\right) \frac{\sin(\theta_\infty)}{\cos(\theta_\infty)^2} \times \frac{1}{s} \tag{2.18}$$

$$v_e = u_w \tan(\theta_\infty)(\alpha \sin(\theta_\infty) + \beta \cos(\theta_\infty)) \tag{2.19}$$

$$\tan(\theta_\infty)^2(\alpha \tan(\theta_\infty) + \beta) = \frac{N_C}{4}. \tag{2.20}$$

Thus, the integral model suggests that, in the far field region, the plume achieves a constant inclination angle (Eq. (2.20)) and a constant velocity (Eq. (2.17)), while the thickness increases linearly with arc length s (Eq. (2.16)) and the excess temperature decreases proportionally to the inverse of s (Eq. (2.18)). Equation (2.20) is the equation for the inclination angle, and this equation suggests that the far-field plume geometry is uniquely determined by Byram’s convection number N_C . Figure 2.4(d) presents the corresponding variations of θ_∞ with N_C : the model predicts that $\theta_\infty \approx 45^\circ$ for $N_C = 2.64$, which may be interpreted as an estimate of the critical value of N_C that delineates between the plume-dominated and wind-driven flame regimes.

In conclusion, consistent with much of the literature, the integral model suggests that Byram’s convection number is the main parameter that controls the structure of wind-aided line fires. Some of the limitations of the integral model are noted: the asymmetry of the air entrainment process is neglected; the presence of solid boundaries is also neglected. Next, we explore further the same configuration and present a series of fine-grained LES, that is, simulations that are not limited by the simplifications made in the integral model.

2.4 Large Eddy Simulations

2.4.1 Numerical Solver

Numerical simulations presented in this section are performed using FireFOAM, a fire modeling solver developed by FM Global and based on an open-source, general-purpose, CFD software package called OpenFOAM³. FireFOAM is a second-order accurate, finite volume solver with implicit time integration; the solver features advanced meshing capabilities (structured or unstructured polyhedral mesh); it also features a massively parallel computing capability using Message Passing Interface protocols.

FireFOAM uses a Favre-filtered, compressible-flow, LES formulation, and provides a choice between several modeling options for the treatment of turbulence, combustion, and thermal radiation. In the baseline configuration: subgrid-scale (SGS) turbulence is described using the one-equation eddy viscosity model, which solves a transport equation for SGS turbulent kinetic energy (Fureby et al. 1997); combustion is described using the classical concept of a global combustion equation combined with the Eddy Dissipation Concept (EDC) model (Magnussen and Hjertager 1976); radiation is described by solving the Radiative Transfer Equation (RTE) using a discrete-ordinates, finite-volume method (Chai and Patanka 2006) and by assuming a nonscattering, nonabsorbing grey medium and using the concept of a prescribed global radiant fraction, χ_{rad} . This baseline configuration was adopted in our past work aimed at simulating an experimental turbulent line burner (Vilfayeau et al. 2016); we refer the reader to Vilfayeau et al. (2016) for details. The only difference between the present modeling choices and the previous baseline configuration is the substitution of the Wall-Adapting Local Eddy-viscosity (WALE) model (Nicoud and Ducros 1999) for the one-equation eddy viscosity model (for SGS turbulence); this model was previously adopted in Ren et al. (2016) and was shown to perform well in the vicinity of solid walls.

2.4.2 Numerical Configuration (with Wind and without Slope)

The numerical configuration is presented in Figure 2.5. The computational domain is 780-cm long in the streamwise x -direction, 50-cm wide in the spanwise y -direction and 250-cm high in the vertical z -direction. The line burner is 5-cm deep in the x -direction and 50-cm wide in the y -direction; the origin $(x, y, z) = (0, 0, 0)$ designates the y -center of the leading edge of the burner. The burner is flush-mounted on a 50-cm wide horizontal solid plate that extends from $x = (-20)$ cm to $x = 205$ cm. The air crossflow is injected through a 50-cm wide and 50-cm

³ OpenFOAM, developed by the OpenFOAM Foundation, available at: www.openfoam.org (last accessed September 29, 2019).

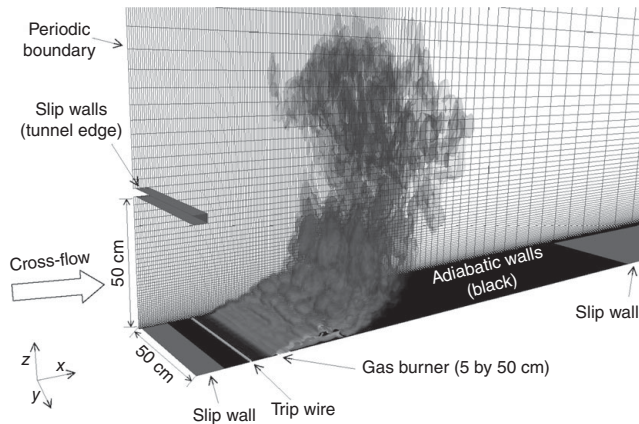


Figure 2.5 General view of the computational domain in LES simulations of the line fire configuration with wind. The burner is 5-cm deep in the x -direction and 50-cm wide in the y -direction; the wind tunnel at the inlet boundary of the computational domain is 50-cm wide in the y -direction and 50-cm high in the vertical z -direction. The flame is visualized using several isocontours of the instantaneous volumetric heat release rate.

A black and white version of this figure will appear in some formats. For the color version, please refer to the plate section.

high wind tunnel located at the inlet boundary of the computational domain, at $x = -30$ cm. Furthermore, a 5-mm deep, 50-cm wide, and 5-mm high trip wire is placed at $x = -10.5$ cm in order to perturb the incoming air flow and to thereby promote laminar-to-turbulent flow transition.

The computational mesh is a rectangular Cartesian grid. For $x \leq 100$ cm, grid spacing in the streamwise x -direction is uniform and equal to 5 mm; beyond that location, the x -grid is stretched with a stretch factor equal to 1.06. Grid spacing in the spanwise y -direction is uniform and is equal to 5 mm. This streamwise (spanwise) resolution corresponds to 10 (100) grid cells across the burner depth (width). Grid spacing in the vertical z -direction is non-uniform: the z -grid spacing is 1.2 mm at $z = 0$ (i.e. the first cell center is located 0.6 mm above the south boundary of the computational domain) and is 20 mm at $z = 50$ cm with a stretching factor of 1.04. For $z > 50$ cm, the z -grid is stretched with a stretch factor equal to 1.06. The total number of cells is 3.5 million.

These choices provide high levels of spatial resolution both in the flame region and in the boundary layer region close to the solid plate surface. The LES simulations are “wall-resolved” (Piomelli and Balaras 2002), that is, the near-wall grid spacing is sufficiently small to accurately capture the gradients of flow velocity at the plate surface and to calculate the wall shear stress directly from the LES solution, without the need for a subgrid-scale wall model. The only exception to the high spatial resolution requirement associated with wall-resolved LES is

made in the trip wire region: the trip wire is under-resolved and is described with one grid cell in the x -direction and four grid cells in the z -direction.

The methane mass flow rate is prescribed at the injection boundary of the burner and the air velocity is prescribed at the vent boundary of the wind tunnel. The horizontal solid plate and the trip wire are both treated as no-slip adiabatic solid walls. The surface located at $z = 0$ between the wind tunnel vent and the leading edge of the solid plate is treated as a slip wall. The surface located at $z = 0$ beyond the solid plate, at $x > 205$ cm, is also treated as a slip wall. The side boundaries at $y = (-25)$ and 25 cm correspond to periodic boundary conditions. Other boundaries correspond to open flow conditions.

In all cases, the methane mass flow rate is linearly increased from 0 to 1 g s^{-1} during the first 5 seconds and is then held constant for the remainder of the simulations. This is done to allow the crossflow to establish itself over the line burner before the heat release rate of the fire reaches its nominal value of 50 kW. At nominal conditions, the fire intensity is $\dot{Q}' = 100 \text{ kW m}^{-1}$. The crosswind velocity is varied between $u_w = 0.75$ and 3 m s^{-1} . Using $\chi_{rad} = 0.23$, these variations in u_w correspond to variations in Byram's convection number between $N_C = 10.2$ and 0.16 . All simulations are performed for a duration of 30 seconds. Turbulent statistics are collected for the final 15 seconds of each simulation, after the flow and flame become statistically stationary and long enough for the statistics to be converged (to improve convergence, statistics are computed using both temporal- and spanwise-averaging). The time step is controlled by a classical Courant-Friedrichs-Lewy (CFL) condition, $\text{CFL} = 0.5$, and is approximately equal to 0.35 ms. Each simulation is run using 200 processors on a large-scale Linux cluster, with a typical simulation requiring 40,000 CPU-hours.

2.4.3 LES Results (Configuration with Wind and without Slope)

Figure 2.6 presents representative results obtained with LES in the form of instantaneous snapshots of the structure of the plume, defined as the region where $(\tilde{T} - T_a) > 100 \text{ K}$. Note that the downstream region in Figure 2.6(c) is affected by reduced resolution due to stretching of the x -grid and should be ignored. As expected, the LES simulations show that at low velocities (that is at $u_w = 0.75 \text{ m s}^{-1}$), the line fire features a vertically tilted, detached geometry, while at high velocities (i.e. at $u_w = 3 \text{ m s}^{-1}$), the fire features a horizontal, attached geometry. In addition, Figure 2.6 shows that as u_w is increased, the turbulent plume evolves from a transitional structure dominated by large-scale two-dimensional motions to a fully-developed turbulent structure dominated by small-scale three-dimensional motions.

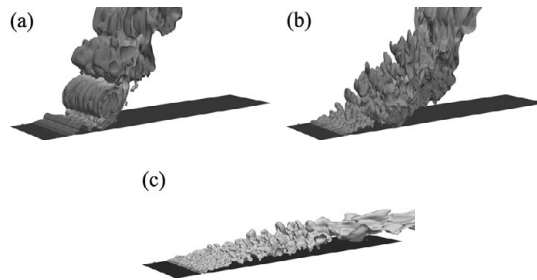


Figure 2.6 LES simulations of the change in flame/plume structure with wind velocity. Three-dimensional instantaneous structure of the plume for different values of the crosswind velocity: (a) $u_w = 0.75 \text{ m s}^{-1}$; (b) $u_w = 1.5 \text{ m s}^{-1}$; (c) $u_w = 3 \text{ m s}^{-1}$. The plume is colored according to the local value of the x -velocity; red (white) corresponds to a low (high) value.

A black and white version of this figure will appear in some formats. For the color version, please refer to the plate section.

Figure 2.7 presents additional results in the form of instantaneous snapshots of the spatial variations of the flow velocity vector and of the flame and plume contours in the central vertical plane of the computational domain; the flame boundary is visualized using an isocontour of the volumetric heat release rate (50 kW m^{-3}); the plume boundary is visualized using an isocontour of temperature ($(\bar{T} - T_a) = 100 \text{ K}$). Note that for ease of visualization, only a subset of the simulated velocity vectors is being plotted in Figure 2.7. For $u_w = 0.75 \text{ m s}^{-1}$, the flow is clearly dominated by the buoyancy of the flame: the cross-flow is strongly deflected in the upward direction; the flow along the wall surface (at $z = 0$) in the region located downwind of the flame is opposed to the wind flow direction, and air entrainment is therefore two-sided. Also, the end of the flame attachment region corresponds to the location where the wall flow separates from the surface (i.e. where the wall boundary layer reverses in flow direction). In contrast, for $u_w = 3.0 \text{ m s}^{-1}$, the flow is now dominated by the momentum of the cross-wind: the cross-flow is only weakly deflected in the upward direction; the flow along the wall surface (at $z = 0$) in the downwind region of the flame is in the wind flow direction and air entrainment is therefore one-sided. As mentioned in Section 2.2, these differences in flow pattern are believed to be key ingredients in flame spread mechanisms (Dold and Zinoviev 2009; Finney et al. 2013, 2015).

Furthermore, a careful observation of the flow pattern presented in Figure 2.7(a) reveals some of the deficiencies in the assumptions made by the integral model discussed in Section 2.3. In the near-field region of the flame, that is, at $x < 30 \text{ cm}$, the flame is clearly strongly affected by the presence of the solid surface and remains attached to that surface. In the far-field region, that is, at $30 \leq x \leq 50 \text{ cm}$,

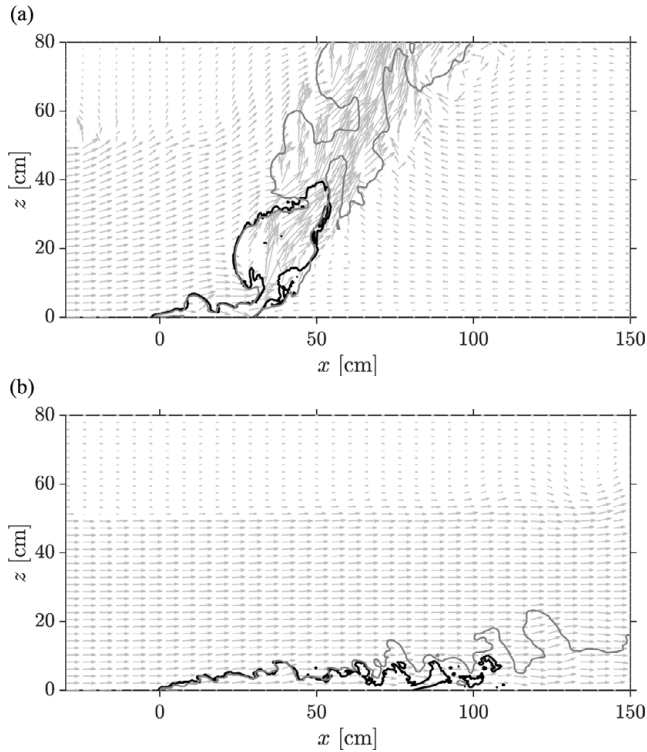


Figure 2.7 LES simulations of the change in flame/plume structure with wind velocity. Two-dimensional instantaneous structure of the flame (solid black line) and plume (solid grey line) for different values of the crosswind velocity: (a) $u_w = 0.75 \text{ m s}^{-1}$; (b) $u_w = 3 \text{ m s}^{-1}$.

the flame is detached from the surface but the flow fields upwind and downwind of the flame are seen to be significantly different and while air entrainment is two-sided, it is likely to be asymmetric with stronger entrainment expected on the upwind side. These observations suggest that the integral model presented in Eqs. (2.4)–(2.9) probably underestimates the deflection of the flame/plume due to wind.

While instantaneous snapshots reveal the rich dynamical content of the LES simulations, relevant information is also obtained by adopting a statistical viewpoint and by analyzing the mean structure of the flame and plume. Figure 2.8 presents the mean (that is, time- and spanwise-averaged) shape and location of the flame and plume, visualized using an isocontour of the mean volumetric heat release rate (50 kW m^{-3}) and an isocontour of the mean temperature ($(\langle \tilde{T} \rangle - T_a) = 100 \text{ K}$), respectively. As u_w increases from 0.75 to 3.0 m s^{-1} , the flame geometry

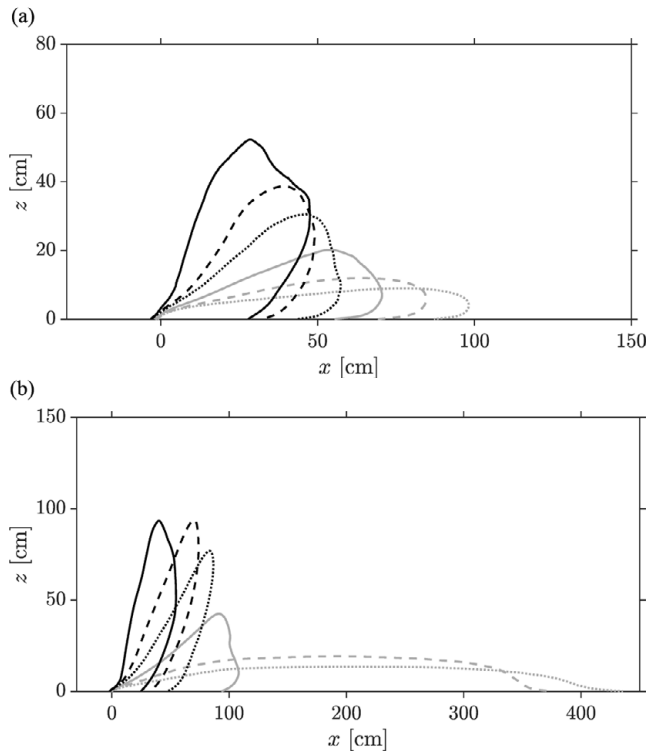


Figure 2.8 LES simulations of the change in flame/plume structure with wind velocity. Two-dimensional mean structure of (a) the flame and (b) the plume. From left to right: $u_w = 0.75, 1.0, 1.25, 1.5, 2.0, 3.0 \text{ m s}^{-1}$.

(Figure 2.8(a)) is seen to evolve from a detached flame regime to an attached flame regime. The vertical elevation of the flame decreases (from 50 to 10 cm); the flame length (loosely defined as the distance from the burner to the flame tip) increases (from 50 to 100 cm); and the flame attachment length (defined as the x -wall-distance downstream of the burner in contact with the flame) increases (from 30 to 90 cm). In the present configuration, the transition from a vertically tilted flame to a horizontal flame is gradual and occurs between $u_w = 1.0$ and 1.5 m s^{-1} . Similar variations are observed in the mean plume shape (Figure 2.8(b)). As u_w increases from 0.75 to 3.0 m s^{-1} , the vertical elevation of the plume decreases (from 90 to 20 cm); the plume length (loosely defined as the distance from the burner to the plume tip) increases (from 90 to 400 cm); and the plume attachment length (defined as the x -wall-distance downstream of the burner in contact with the plume) increases (from 30 to 400 cm). The transition from a vertically tilted plume to an elongated horizontal plume is abrupt and occurs between $u_w = 1.5$ and 2.0 m s^{-1} .

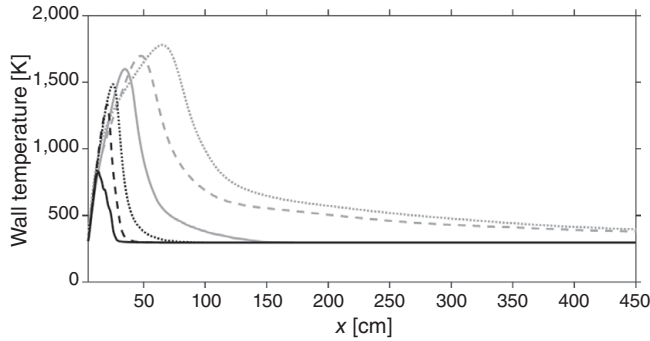


Figure 2.9 LES simulations of the change in flame/plume structure with wind velocity. Variations of the mean wall temperature with spatial distance. From left to right: $u_w = 0.75, 1.0, 1.25, 1.5, 2.0, 3.0 \text{ m s}^{-1}$.

Additional information on the flame and plume attachment behavior is presented in Figure 2.9, which plots the spatial variations of the mean temperature along the (adiabatic) wall surface. In this figure, the flame attachment region can be identified as the region where the mean wall temperature increases; the plume attachment region is the region located downstream, beyond the point where the mean wall temperature reaches a maximum value. As mentioned in the discussion of Figure 2.8, as u_w increases from 0.75 to 3.0 m s^{-1} , the simulations predict a gradual increase in the flame attachment length as well as an abrupt increase in the plume attachment length for u_w between 1.5 and 2.0 m s^{-1} . The simulations also predict a gradual increase in the peak value of the mean wall temperature. Assuming that convection (rather than radiation) is the dominant heat transfer mechanism, the length of the region where the mean wall temperature is higher than 600 K (taken here as a representative value for the start of pyrolysis in typical vegetation fuel) can be interpreted as giving an estimate of the length of the preheating region in a flame spread scenario.

The LES results can be compared to the predictions of the integral model discussed in Section 2.3. For comparison purposes, the mean plume shape simulated by LES is characterized as follows (Figure 2.10): first the plume attachment length, $x_{p,a}$, is calculated as the x -wall-distance downstream of the burner in contact with the plume (where $\langle \tilde{T} \rangle - T_a > 100 \text{ K}$); point B is then defined as the mid-point of the base of the plume at $z = 0$, that is, as the point of coordinates $(x, z) = (0.5 \times x_{p,a}, 0)$; next, the tip point T is defined as the point on the plume edge contour that is located at the maximum distance from B (note that this definition is preferred to a definition of T as the point on the plume edge contour with maximum elevation; the two definitions are similar in the case of detached plumes but the present definition provides a better description of the

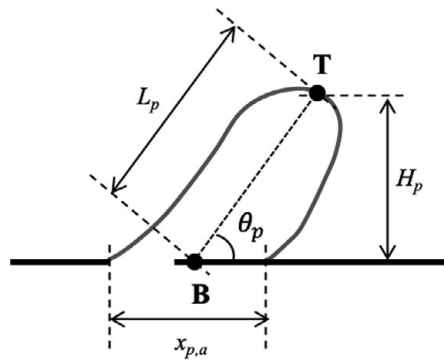


Figure 2.10 Analysis of the mean plume shape simulated by LES. Point B is the mid-point of the base of the plume; point T is the tip of the plume; θ_p is the plume inclination angle.

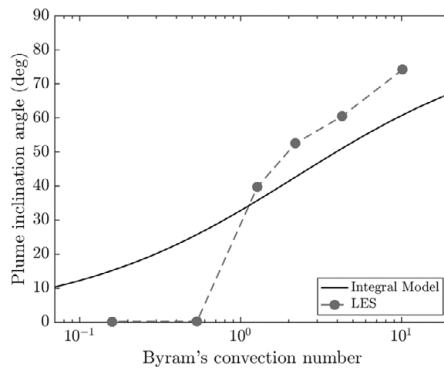


Figure 2.11 Variations of the plume inclination angle, θ_p , with Byram's convection number, N_C . Comparison between results obtained with the integral model (solid line) and with LES (dashed line with dot symbols).

plume shape in the case of attached plumes); the line that connects B to T allows us to define the plume length, L_p , and plume vertical height, H_p ; finally, the plume inclination angle θ_p is obtained as the angle between the B–T line and the horizontal plane.

Figure 2.11 presents the variations of the plume inclination angle, θ_p , with the crosswind velocity, u_w , re-cast in the form of Byram's convection number N_C . The figure compares predictions obtained with the integral model discussed in Section 2.3 and with LES. The LES data suggests that the transition between the attached plume regime ($\theta_p = 0$) and the detached plume regime ($\theta_p > 0$) is abrupt and occurs for a value of N_C between 0.5 ($u_w = 2 \text{ m s}^{-1}$) and 1.3 ($u_w = 1.5 \text{ m s}^{-1}$). In the detached plume regime ($N_C \geq 1.3$, $u_w \leq 1.5 \text{ m s}^{-1}$), the comparison

between predictions by the integral model and by LES is relatively good: the values of θ_p obtained in the integral model are within 10 degrees of the LES values. The integral model, however, does not capture the transition to the attached plume regime observed in the LES at low values of N_C ($N_C \leq 0.5, u_w \geq 2 \text{ m s}^{-1}$). Recall that these results are obtained for a fixed value of the fire intensity, $\dot{Q}' = 100 \text{ kW m}^{-1}$; additional simulations (not shown here) performed with different values of the fire intensity, $\dot{Q}' = 20$ and 500 kW m^{-1} , confirm that the transition between the plume-dominated and wind-driven line fires occurs for a critical value of Byram's convection number between 0.5 and 2.

2.4.4 Numerical Configuration (with Slope and without Wind)

The numerical configuration is presented in Figure 2.12. The computational domain is first constructed at zero slope angle with the same grid spacing and dimensions already used in the wind-aided configuration, except that the burner location, that is, the origin $(x, y, z) = (0, 0, 0)$, is now placed at equal distance from the x -boundaries, and that the trip wire and the wind tunnel are removed. The domain is then tilted to model different slope angles while keeping the grid lines normal or parallel to the inclined surface. The heat release rate of the fire is 50 kW ; the fire intensity is $\dot{Q}' = 100 \text{ kW m}^{-1}$.



Figure 2.12 General view of the computational domain in LES simulations of the line fire configuration with slope. The computational mesh is tilted so that grid lines remain normal or parallel to the inclined surface. The flame is visualized using volume rendering of temperature.

A black and white version of this figure will appear in some formats. For the color version, please refer to the plate section.

2.4.5 LES Results (Configuration with Slope and without Wind)

Figure 2.13 presents instantaneous snapshots of the spatial variations of the flow velocity vector plotted with the flame and plume contours in the central vertical plane of the computational domain; the flame and plume contours are visualized using the same methodology already used in Figure 2.7. For $\theta_s = 18$ degrees, the flow is clearly dominated by vertical motions: the flame and plume are detached from the surface; the flow direction upslope of the flame is opposed to the flow direction downslope of the flame and air entrainment is two-sided. In contrast, for $\theta_s = 36$ degrees, the flow is now dominated by strong upslope motions: the flame and plume feature a boundary layer geometry; the flow along the wall surface

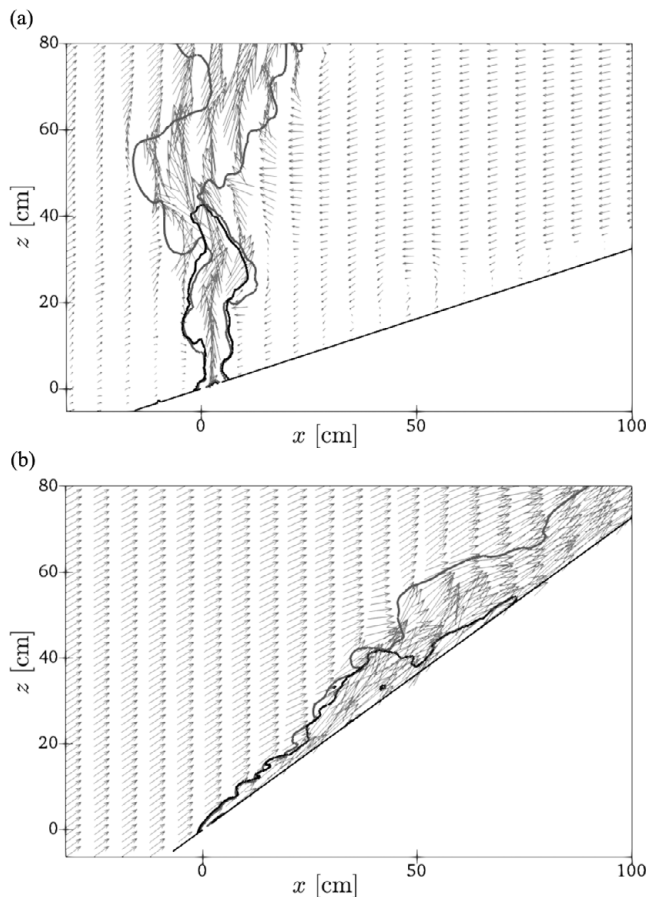


Figure 2.13 LES simulations of the change in flame/plume structure with slope angle. Two-dimensional instantaneous structure of the flame (solid black line) and plume (solid grey line) for different values of the slope angle: (a) $\theta_s = 18$ degrees; (b) $\theta_s = 36$ degrees.

remains in the upslope direction and air entrainment is therefore one-sided. The strong difference in the air entrainment process observed when comparing Figures 2.13(a) and 2.13(b) illustrates the concept of an effective wind created by the line fire when developing along an inclined surface: while for $\theta_s = 18$ degrees, the mean entrainment velocity measured downslope of the flame is on the order of 0.3 m s^{-1} , this velocity is more than doubled for $\theta_s = 36$ degrees. This increase in the downslope entrainment velocity is associated with, and can be explained by, the effects of wall blockage and the corresponding reduction in entrainment velocity occurring on the upslope side of the flame.

Figure 2.14 presents the mean (i.e. time- and spanwise-averaged) shape and location of the flame and plume; the mean flame and plume contours are visualized using the same methodology already used in Figure 2.8; in contrast to the choice made in Figure 2.13, the contours are now presented in a tilted plane attached to the inclined surface. As θ_s increases from 9 to 36 degrees, the flame geometry (Figure 2.14(a)) is seen to evolve from a detached flame regime to an attached flame regime. The normal (i.e. normal to the wall surface) elevation of the flame decreases (from 60 to 10 cm); the flame length increases (from 60 to 100 cm); and

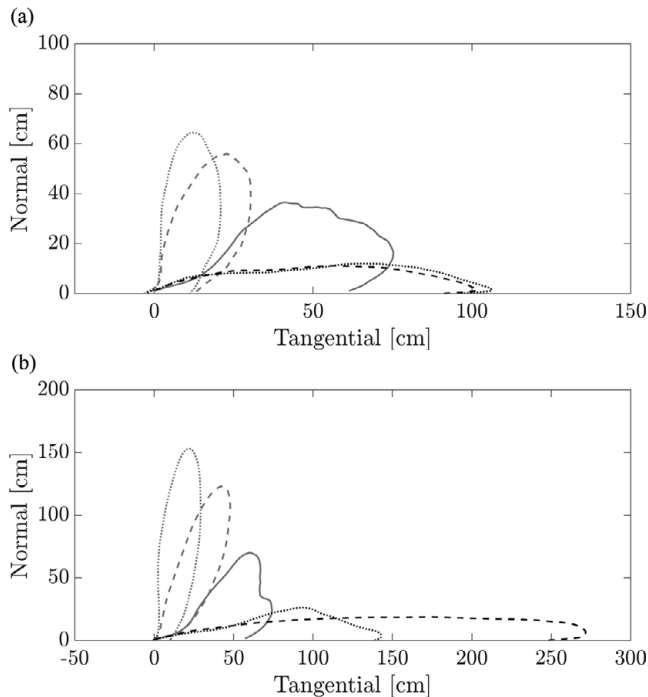


Figure 2.14 LES simulations of the change in flame/plume structure with slope angle. Two-dimensional mean structure of (a) the flame and (b) the plume. From left to right: $\theta_s = 9, 18, 24, 30, 36$ degrees.

the flame attachment length increases (from 10 to 100 cm). In the present configuration, the transition from a vertically tilted flame to a wall flame is abrupt and occurs between $\theta_s = 18$ and 30 degrees, approximately at $\theta_s \approx 24$ degrees. Similar variations are observed in the mean plume shape (Figure 2.14(b)). As θ_s increases from 9 to 36 degrees, the normal elevation of the plume decreases (from 150 to 20 cm); the plume length increases (from 150 to 270 cm); and the plume attachment length increases (from 10 to 250 cm). The transition from a vertically tilted plume to an elongated wall plume is abrupt and occurs approximately at $\theta_s \approx 24$ degrees.

2.5 Conclusion

Fine-grained LES are presented in this chapter to bring fundamental insight into the effects of crosswind or sloped terrain on the structure of buoyancy-driven, turbulent line fires. The LES simulations describe the transition between a pool-like, detached flame geometry, characterized by a tilted vertical shape, and a boundary layer, attached flame geometry, characterized by a wall-attached shape. The detached flames feature downwind/upslope flow separation and two-sided air entrainment into the flame. In contrast, the attached flames feature unidirectional flow and one-sided air entrainment into the flame. The analysis of the LES results is supported by an integral model that helps identify the dominant parameters that control the transition between the detached and attached flame/plume regimes.

The present flame configurations are simplified: the flames are gas-fueled, correspond to a small fixed value of the burner width, and are statistically two-dimensional (i.e. they correspond to line fires developing in “trenches” or in “canyons”); in addition, the flames correspond to weak-to-moderate fires (the fire intensities are below 500 kW m^{-1}). In these simplified configurations, the transition between the two flame regimes is observed for a critical value of Byram’s convection number N_C close to 1 in the case of wind-aided flames, and for a critical value of the slope angle θ_s close to 24 degrees in the case of slope-aided flames. There is a need to confirm the present results in configurations featuring a range of values of the burner width as well as larger values of the fire intensity.

Future research should also be directed at extending the reach of detailed analysis to the case of flames propagating over representative vegetation beds. One objective is to bring higher fidelity to the geometric description of the fuel sources, in particular through a treatment of the vegetation fuel as a discontinuous system with effects associated with fuel particle size distributions and separation distances. Another objective is to bring higher fidelity to the description of flame spread dynamics through a treatment of the uncontrolled production of flammable

vapors due to pyrolysis processes and to the gas-to-solid heat transfer as well as a treatment of the typical cycle of ignition, pyrolysis and end-of-pyrolysis/burn-out. And finally, a related objective is to bring higher fidelity to the description of flame spread dynamics through a treatment of the displacement of the flame.

References

- Albini, FA (1981) A model for the wind-blown flame from a line fire. *Combustion and Flame* **43**, 155–174.
- Canfield, JM, Linn, RR, Sauer, JA, Finney, M, Forthofer, J (2014) A numerical investigation of the interplay between fireline length, geometry, and rate of spread. *Agricultural and Forest Meteorology* **189–190**, 48–49.
- Chai, J, Patanka, S (2006) Discrete-ordinates and finite-volume methods for radiation heat transfer. In: Minkowycz, WJ, Sparrow, EM, Murthy, JY, eds. *Handbook of Numerical Heat Transfer*. Hoboken, NJ: John Wiley & Sons, pp. 297–323.
- Clark, TL, Coen, J, Latham, D (2004) Description of a coupled atmosphere–fire model. *International Journal of Wildland Fire* **13**(1), 49–64.
- Coen, JL, Cameron, M, Michalakes, J, Patton, EG, Riggan, PJ, Yedinak, KM. (2013) Wrf-fire: Coupled weather–wildland fire modeling with the weather research and forecasting model. *Journal of Applied Meteorology and Climatology* **52**(1), 16–38.
- Dold, JW, Zinoviev, A (2009) Fire eruption through intensity and spread rate interaction mediated by flow attachment. *Combustion Theory and Modelling* **13**(5), 763–793.
- Drysdale, DD, Macmillan, AJR (1992) Flame spread on inclined surfaces. *Fire Safety Journal* **18**, 245–254.
- Dupuy, J-L, Maréchal, J (2011) Slope effect on laboratory fire spread: Contribution of radiation and convection to fuel bed preheating. *International Journal of Wildland Fire* **20**(2), 289–307.
- Dupuy, J-L, Maréchal, J, Portier, D, Valette, J-C (2011) The effects of slope and fuel bed width on laboratory fire behaviour. *International Journal of Wildland Fire* **20**(2), 272–288.
- Escudier, MP (1972) Aerodynamics of a burning turbulent gas jet in a crossflow. *Combustion Science and Technology* **4**(1), 293–301.
- Escudier, MP (1975) Analysis and observations of inclined turbulent flame plumes. *Combustion Science and Technology* **10**(3–4), 163–171.
- Filippi, JB, Bosseur, F, Mari, C, Lac, C, Moigne, PL, Cuenot, B, Veynante, D, Cariolle, D, Balbi, J (2009) Coupled atmosphere–wildland fire modelling. *Journal of Advances in Modeling Earth Systems* **1**(4), 11.
- Filippi, JB, Pialat, X, Clements, CB (2013) Assessment of forefire/meso-nh for wildland fire/atmosphere coupled simulation of the fireflux experiment. *Proceedings of the Combustion Institute* **34**(2), 2633–2640.
- Finney, MA, Cohen, JD, Forthofer, JM, McAllister, SS, Gollner, MJ, Gorham, DJ, Saito, K, Akafuah, NK, Adam, BA, English, JD. (2015) Role of buoyant flame dynamics in wildfire spread. *Proceedings of the National Academy of Sciences (USA)* **112**(32), 9833–9838.
- Finney, MA, Cohen, JD, McAllister, SS, Jolly, WM (2013) On the need for a theory of wildland fire spread. *International Journal of Wildland Fire* **22**(1), 25–36.
- Fureby, C, Tabor, G, Weller, HG, Gosman, AD (1997) A comparative study of subgrid scale models in homogeneous isotropic turbulence. *Physics of Fluids* **9**(5), 1416–1429.

- Hoult, DP, Fay, JA, Forney, LJ (1969) A theory of plume rise compared with field observations. *Journal of the Air Pollution Control Association* **19**(8), 585–590.
- Hu, L (2017) A review of physics and correlations of pool fire behaviour in wind and future challenges. *Fire Safety Journal* **91**, 41–55.
- Huang, X, Gollner, MJ (2014) Correlations for evaluation of flame spread over an inclined surface. *Proceedings of the Eleventh International Symposium, International Association for Fire Safety Science (IAFSS)* **13**, 222–233.
- Kochanski, AK, Jenkins, MA, Mandel, J, Beezley, JD, Clements, CB, Krueger, S (2013) Evaluation of wrf-sfire performance with field observations from the fireflux experiment. *Geoscientific Model Development* **6**(4), 1109–1126.
- Krishnamurthy, R, Hall, JD (1987) Numerical and approximate solutions for plume rise. *Atmospheric Environment* **21**(10), 2083–2089.
- Lam, CS, Weckman, EJ (2015a) Wind-blown pool fire, Part I: Experimental characterization of the thermal field. *Fire Safety Journal* **75**, 1–13.
- Lam, CS, Weckman, EJ (2015b) Wind-blown pool fire, Part II: Comparison of measured flame geometry with semi-empirical correlations. *Fire Safety Journal* **78**, 130–141.
- Linn, RR, Cunningham, P (2005) Numerical simulations of grass fires using a coupled atmosphere-fire model: Basic fire behavior and dependence on wind speed. *Journal of Geophysical Research* **110**, D13107.
- Magnussen, BF, Hjertager, BH (1976) On mathematical modeling of turbulent combustion with special emphasis on soot formation and combustion. *Symposium (International) on Combustion* **16**(1), 719–729.
- Mandel, J, Beezley, JD, Kochanski, AK (2011) Coupled atmosphere-wildland fire modeling with wrf 3.3 and sfire 2011. *Geoscientific Model Development* **4**(3), 591–610.
- Mell, W, Jenkins, MA, Gould, J, Cheney, P (2007) A physics-based approach to modeling grassland fires. *International Journal of Wildland Fire* **16**(1), 1–22.
- Mercer, GN, Weber, RO (1994) Plumes above line fires in a cross wind. *International Journal of Wildland Fire* **4**(4), 201–207.
- Morandini, F, Silvani, X (2010) Experimental investigation of the physical mechanisms governing the spread of wildfires. *International Journal of Wildland Fire* **19**(5), 570–582.
- Morandini, F, Silvani, X, Dupuy, J-L, Susset, A (2018) Fire spread across a sloping fuel bed: Flame dynamics and heat transfers. *Combustion and Flame* **190**, 158–170.
- Morvan, D (2011) Physical phenomena and length scales governing the behavior of wildfires: A case for physical modelling. *Fire Technology* **47**(2), 437–460.
- Morvan, D, Dupuy, JL (2001) Modeling of fire spread through a forest fuel bed using a multiphase formulation. *Combustion and Flame* **127**(1–2), 1981–1994.
- Morvan, D, Dupuy, JL (2004) Modeling the propagation of a wildfire through a mediterranean shrub using a multiphase formulation, *Combustion and Flame* **138**(3), 199–210.
- Morvan, D, Frangieh, N (2008) Wildland fires behavior: Wind effect versus Byram's convective number and consequences upon the regime of propagation. *International Journal of Wildland Fire* **27**(9), 636–641.
- Morvan, D, Porterie, B, Larini, M, Loraud, JC. (1998) Numerical simulation of turbulent diffusion flame in cross flow. *Combustion Science and Technology* **140**(1–6), 93–122.
- Nelson, RM (1993) Byram's derivation of the energy criterion for forest and wildland fires. *International Journal of Wildland Fire* **3**(3), 131–138.
- Nelson, RM (2002) An effective wind speed for models of fire spread. *International Journal of Wildland Fire* **11**(2), 153–161.

- Nelson, RM (2015) Re-analysis of wind and slope effects on flame characteristics of Mediterranean shrub fires. *International Journal of Wildland Fire* **24**(7), 1001–1007.
- Nelson, RM, Butler, BW, Weise, DR (2012) Entrainment regimes and flame characteristics of wildland fires. *International Journal of Wildland Fire* **21**(2), 127–140.
- Nicoud, F, Ducros, F (1999) Subgrid-scale stress modelling based on the square of the velocity gradient tensor. *Flow, Turbulence and Combustion* **62**(3), 183–200.
- Nmira, F, Consalvi, JL, Boulet, P, Porterie, B (2010) Numerical study of wind effects on the characteristics of flames from non-propagating vegetation fires. *Fire Safety Journal* **45**(2), 129–141.
- Pagni, PJ, Peterson, TG (1973) Flame spread through porous fuels. *Symposium (International) on Combustion* **14**(1), 1099–1107.
- Piomelli, U, Balaras, E (2002) Wall-layer models for large-eddy simulations. *Annual Review of Fluid Mechanics* **34**, 349–374.
- Porterie, B, Morvan, D, Loraud, JC, Larini, M (2000) Firespread through fuel beds: Modeling of wind-aided fires and induced hydrodynamics. *Physics of Fluids* **12**(7), 1762–1782.
- Putnam, AA (1965) A model study of wind-blown free-burning fires. *Symposium (International) on Combustion* **10**(1), 1039–1046.
- Raupach, MR (1990) Similarity analysis of the interactions of bushfire plumes with ambient winds. *Mathematical and Computer Modelling* **13**(12), 113–121.
- Ren, N, Wang, Y, Vilfayeau, S, Trouvé, A (2016) Large eddy simulation of turbulent vertical wall fires supplied with gaseous fuel through porous burners. *Combustion and Flame* **169**(3), 194–208.
- Sharples, JJ, Gill, AM, Dold, JW (2010) The trench effect and eruptive wildfires: Lessons from the King's Cross underground disaster. *Proceedings of the Australasian Fire and Emergency Service Authorities Council (AFAC) Conference*, September, Darwin.
- Smith, DA (1992) Measurements of flame length and flame angle in an inclined trench. *Fire Safety Journal* **18**(3), 231–244.
- Sullivan, AL (2007) Convective froude number and Byram's energy criterion of Australian experimental grassland fires. *Proceedings of the Combustion Institute* **31**(2), 2557–2564.
- Tang, W, Miller, CH, Gollner, MJ (2017) Local flame attachment and heat fluxes in wind-driven line fires. *Proceedings of the Combustion Institute* **36**(2), 3253–3261.
- Viegas, DX (2004) On the existence of a steady state regime for slope and wind driven fires. *International Journal of Wildland Fire* **13**(1), 101–117.
- Viegas, DX (2005) A mathematical model for forest fires blowup. *Combustion Science and Technology* **177**(1), 27–51.
- Vilfayeau, S, White, JP, Sunderland, PB, Marshall, AW, Trouvé, A (2016) Large eddy simulation of flame extinction in a turbulent line fire exposed to air–nitrogen co-flow. *Fire Safety Journal* **86**, 16–31.
- Woodburn, PJ, Drysdale, DD (1998) Fires in inclined trenches: The dependence of the critical angle on the trench and burner geometry. *Fire Safety Journal* **31**, 143–164.
- Wu, Y, Xing, HJ, Atkinson, G (2000) Interaction of fire plume with inclined surface. *Fire Safety Journal* **35**(4), 391–403.
- Yuan, L-M, Cox, G (1996) An experimental study of some line fires. *Fire Safety Journal* **27**(2), 123–139.